Volume 18, Number 4, 2025. pp. 497-516

Jordan Journal of Physics

ARTICLE

Reuse of Waste Glass Doped with Agricultural and Mining Wastes as Radiation Shielding Materials: A Computational and Experimental Study

Zeynep AYGUN[a] and **Murat AYGUN**[b]

[a] *Vocational School of Technical Sciences, Bitlis Eren University, 13100, Bitlis, Turkey.*

[b] *Department of Physics, Faculty of Science and Arts, Bitlis Eren University, 13100, Bitlis, Turkey.*

Doi: **https://doi.org/10.47011/18.4.8**

Received on: 16/07/2024; *Accepted on: 20/01/2025*

Abstract: The objective of the study is to reuse the waste materials generated from daily household activities, as well as food and mining industries, and to determine the radiation shielding capabilities of materials produced from these wastes. In this context, four groups of waste samples were prepared using various combinations of waste glass, agricultural wastes, and mining wastes, including tea waste, eggshell waste, peanut shell waste, tincal waste, Bayburt stone waste, and green clay, mixed in different ratios. The effects of adding Ta and W to these waste-based composites on their shielding performance were also examined. The Phy-X/PSD, a widely used code, was applied to calculate the radiation protection parameters. In addition, spectroscopic results were provided based on X-ray diffraction (XRD), electron paramagnetic resonance (EPR), scanning electron microscopy (SEM), and energy dispersive spectroscopy techniques. The results of the shielding parameter analysis revealed that all prepared samples exhibited radiation shielding capability, with the second and third samples showing superior performance. The highest mass attenuation cross-section value at 0.015 MeV was observed for sample B3 (comprising waste glass, Bayburt stone waste, eggshell waste, and tungsten), measured at 34.960 cm^2g^{-1}, while the lowest value was found for sample X1 (comprising waste glass, tincal waste, and green clay), measured at 7.704 cm^2g^{-1}. A clear relationship was observed between the content of tantalum, tungsten, and eggshell waste and the radiation protection capacities of the samples. It can also be noted that the neutron shielding abilities of the samples were found to be consistent with their photon shielding properties. For sample B3, the α-W main phase at ≈40° exhibited a crystallite size of 41.51 nm, suggesting that structures with larger crystallite sizes demonstrate better shielding performance. Overall, it can be concluded that the newly developed waste-based composites show promising radiation protection characteristics. Their use as alternative materials in place of cement, aggregate, or concrete can be recommended to promote recycling and sustainable material reuse.

Keywords: Waste glass, Waste types, Phy-X/PSD, Radiation shielding capability.

PACS: 28.41.Qb, 91.62.Rt.

1. Introduction

The use of complementary cementitious materials (CCMs) to partially replace cement in concrete has recently become a widely adopted approach to mitigate the negative environmental impacts of industrial activities. Various industrial by-products have been successfully used as CCMs [1, 2]. The addition of the materials into cement can improve the durability, strength, and workability of concrete while also offering economic benefits [3]. Among these by-

Corresponding Author: Zeynep AYGUN **Email**: zeynep.yarbasi@gmail.com

products, waste glass has emerged as a candidate for use as a CCM. Waste glass has become a bigger problem as consumption increases with the increasing population all over the world. Implementing and increasing technologies for waste recycling and reuse has become a global need to focus on. Although recycling technologies are used, a high amount of waste glass is still awaiting evaluation [4]. As seen in several studies, waste glass is thought to be suitable for use as aggregate based on its characteristics and chemical composition similar to conventional CCMs [5-8]. It was reported by Kim *et al.* [5] that incorporating waste glass enhances the durability and radiation shielding performance of mortar. Binici *et al.* [6] studied the effect of eggshells on radiation shielding efficiency and concluded that their inclusion improved the protective capacity of the samples. Given its abundance and low cost, waste glass can also serve as a practical replacement for cement in concrete production [9, 10]. Taha and Nouna [10] examined the use of recycled glass in concrete as both sand and pozzolanic powder and stated that there is not much difference in compressive strength of concrete with the presence of recycled glass sand as sand replacement.

Although concrete possesses many favorable properties, it also has certain drawbacks, such as a lack of optical transparency and a reduction in mechanical strength when exposed to radiation. In this context, glass is a type of radiation shield material that can be an alternative to concrete due to its optical transparency, ease of manufacturing, non-toxicity, low cost, and physical and chemical properties. Radiation protection properties can be changed and improved by adding different materials to the glass. Soda-lime-silica (SLS) glass is a type of glass used generally in glass containers or window glass, such as bottles and jars, and is often employed as an alternative SiO_2 source. SLS glass typically appears in green or brown colors and contains elements such as Si, Na, Ca, Mg, Al, and Fe. In addition, waste materials rich in silica and calcium—such as eggshells, peanut shells, tincal waste, Bayburt stone waste, and different types of clay—can be reused to minimize environmental impact and provide economic benefits [11].

Cement production, on the other hand, is energy-intensive, costly, and associated with significant CO_2 emissions. Therefore, limestone-based materials can serve as effective fillers in concrete, among which eggshells are a viable option [12]. Other industrial waste materials, including tincal waste [13], Bayburt stone waste [14], and clay types [12], possess good refractory properties and can be recycled or repurposed as building materials. Furthermore, waste composites can be doped with heavy elements or oxides such as W, Ta, and WO_3 to enhance their radiation shielding capabilities [15, 16]. Materials containing tungsten (W) and tantalum (Ta) are characterized by a superior shielding effect due to the high atomic number and high density properties of W (Z:74, ρ:19.3) and Ta (Z:73, ρ:16.67) [16]. W and Ta are considered effective and non-toxic alternatives to lead, offering additional advantages such as high melting points, low neutron activation, and superior thermal conductivity. Moreover, Ta doping contributes to improved tensile strength at elevated temperatures [16].

Although radiation offers numerous benefits and is widely used in fields such as science, industry, agriculture, energy, medicine, and radiology, prolonged or excessive exposure can lead to serious short- and long-term health problems for individuals who work in or receive services from these sectors. Consequently, protection against the harmful effects of radiation on all forms of living organisms has become an increasingly important research focus. Recent studies have concentrated on developing shielding materials with enhanced radiation absorption capabilities. Various materials, such as glass, rock, composites, thin films, polymers, and concrete, have been investigated for this purpose, particularly those that are novel, non-toxic, cost-effective, and lightweight [4–6, 16–21]. Eid *et al.* [4] investigated the effects of adding waste glass into cement to evaluate its radiation shielding properties and found that this approach not only improves shielding performance but also supports waste reuse. Aygun *et al.* [18] reported good radiation protection performance for green and red clays reinforced with waste tire and marble dust residues. Elsafi *et al.* [19] studied the radiation shielding properties of a newly developed eco-friendly epoxy composite containing waste marble and WO3, and stated that it exhibited superior radiation protection compared to other polymers. Effective radiation-shielding materials can be developed by optimizing parameters such as attenuation capability, environmental friendliness, and sustainability, aiming to reduce both radiation exposure and environmental pollution.

The minimization and recycling of waste materials are fundamental aspects of an effective waste management strategy. The protection of natural resources, diminishing the necessity for raw materials to manufacture new products, reducing environmental pollution, providing opportunities for new employment, and decreasing energy consumption are some of the advantages of preferring waste materials. In this context, the motivation of the study is to produce materials with strong radiation shielding performance using waste glass and other types of waste generated from daily household activities and various industries. Accordingly, the exposure and energy absorption buildup factors (EBF and EABF), linear attenuation coefficients (LAC), mass attenuation coefficients (MAC), effective atomic number (Z_eff), mean free path (MFP), half-value layer (HVL), and fast neutron removal cross-section (FNRCS), i.e. the key shielding parameters, were calculated for samples containing different proportions of waste glass (WG), green clay (GC), peanut shell waste (PSW), waste tea (WT), eggshell waste (ESW), tincal waste (TW), and Bayburt stone waste (BSW) using the Phy-X/PSD code [22]. The prepared samples were also analyzed by spectroscopic techniques, as well as their shielding abilities. X-ray diffraction (XRD) was performed to ascertain the crystalline phases or amorphous structure of the samples. Electron paramagnetic resonance (EPR) was used to investigate the magnetic features of the systems by applying a microwave frequency and an external magnetic field. Scanning electron microscopy (SEM) provided information on surface morphology, while energy-dispersive spectroscopy (EDS) was used to determine elemental composition.

The development of non-toxic and effective materials is a requirement of effective radiation protection. While meeting this requirement, it is desirable that such materials are environmentally friendly and contribute to reducing pollution. For this purpose, this study demonstrates that waste materials generated both in households and in the food and beverage industry can be repurposed as substitutes for cement, aggregate, or concrete, offering promising protective properties. By investigating newly developed waste-based materials, this work provides valuable insights into the potential reuse of waste glass and other types of waste as effective radiation shielding materials.

2. Materials and Methods

2.1. Sample Preparation

Four kinds of samples were produced and designated as the S group (S1, S2, S3), B group (B1, B2, B3), A group (A1, A2, A3), and X group (X1, X2, X3). The waste components used in the samples included waste glass (WG), green clay (GC), peanut shell waste (PSW), waste tea (WT), eggshell waste (ESW), tincal waste (TW), and Bayburt stone waste (BSW). The proportions of these components in each sample group are presented in Table 1. Initially, the waste glass and other waste materials were ground into fine powders, measured in specified quantities, and placed in porcelain crucibles. The mixtures were then melted in a furnace at 1100 °C for 2 hours, followed by heat treatment at 500 °C for 3 hours. Finally, the furnace was turned off, and the glass samples were allowed to cool naturally to room temperature. The resulting glass samples were subsequently crushed and prepared for experimental analysis. The sample preparation procedure is demonstrated in Fig. 1.

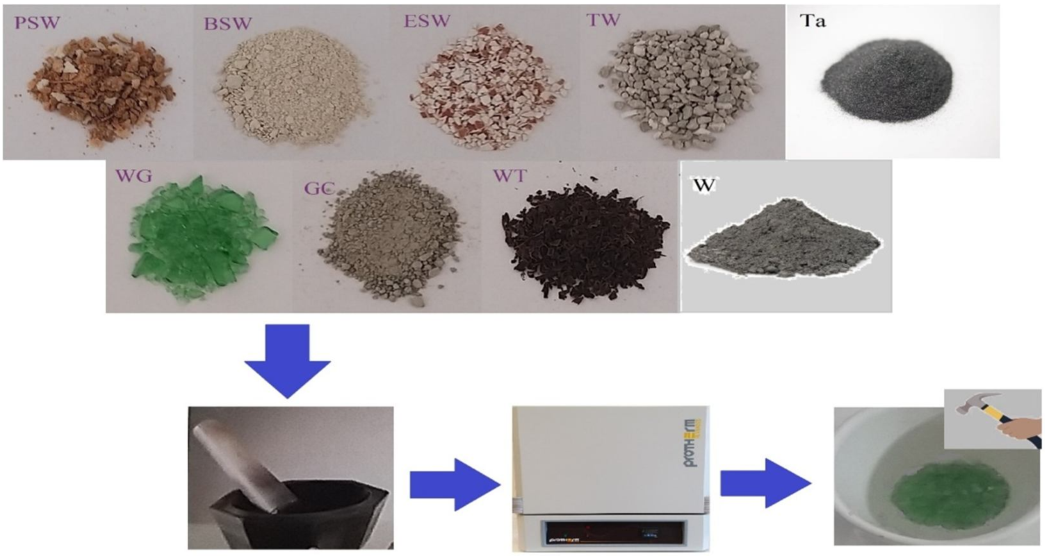

FIG. 1. Procedure of sample preparation.

TABLE 1. Compositional rate of the prepared samples.

S group	WG (%)	ESW (%)	PSW (%)	Ta (%)	W (%)
S1	80	10	10	-	-
S2	70	10	10	10	-
S3	75	10	10	-	5
B group	WG	BSW	ESW	Ta	W
B1	80	10	10	-	-
B2	70	10	10	10	-
B3	75	10	10	-	5
A group	WG	ESW	WT	Ta	W
A1	90	5	5	-	-
A2	90	4	4	2	-
A3	90	4.5	4.5	-	1
X group	WG	TW	GC	Ta	W
X1	90	5	5	-	-
X2	90	4	4	2	-
X3	90	4.5	4.5	-	1

2.2. Experimental Techniques

Room temperature EPR spectra were taken by X-band JEOL JESFA300 EPR spectrometer operating at ≈ 9.2 GHz frequency with a 100 kHz (0.0002-2mT) magnetic field modulation amplitude. A 4 mm diamagnetic tube was used for the EPR experiment. XRD patterns were taken by BRUKER D8 ADVANCE XRD. XRD results of the samples were recorded with 2.5°/min (40 kV and 40 mA) scanning speed in the range of $2\Theta \approx 10°-90°$ by Cu-Kα (λ = 1.54060 Å) at room temperature. SEM images were recorded by ZEISS EVO LS10. EDS was performed with a JEOL JSM-6610 spectrometer at room temperature. Powder samples illustrated in Fig. 1 were used in all experimental techniques.

2.3. Theoretical Process

The calculation of radiation shielding parameters using the Phy-X/PSD code begins by entering the material composition, which can be defined either in terms of weight fraction or mole fraction. For the determination of the attenuation parameters, material density (g/cm^3) is also necessary. The obtained results are supplied in an MS Excel file. For detailed information on the Phy-X/PSD code and the attenuation parameters, readers are referred to the work of Sakar *et al.* [22].

The rule of mixtures was used to determine the density (ρ_{mix}) of the samples [23]:

$$\rho_{mix} = \frac{\sum_{i=1}^{n} c_i A_i}{\frac{\sum_{i=1}^{n} c_i A_i}{\rho_i}} \tag{1}$$

where c_i, A_i, and ρ_i are the atomic weight of element i_{th}, atomic fraction, and density, respectively.

The MAC can be determined based on the Beer–Lambert law as:

$$I = I_0 e^{-\mu t} \tag{2}$$

$$\mu_m = \frac{\mu}{\rho} = ln(I_0/I)/\rho t = ln(I_0/I)/t_m \tag{3}$$

where t_m (g/cm^2), t (cm), μ(cm^{-1}), and μ_m(cm^2/g) are the sample mass thickness, thickness (the mass per unit area), LAC, and MAC, respectively.

The MAC for any compound can also be found by the following equation [24]:

$$\mu/\rho = \sum_i w_i \, (\mu/\rho)_i \tag{4}$$

where $(\mu/\rho)_i$ and w_i are the MAC of the ith constituent element and the weight fraction, respectively.

The HVL is the thickness of the material required to halve the amount of incident radiation, and the MFP is the distance traveled by a photon between two consecutive collisions. The MFP and HVL can be determined by the formulas [22]

$$MFP = \frac{1}{\mu} \tag{5}$$

$$HVL = \frac{In(2)}{\mu} \tag{6}$$

The atomic cross-section (ACS), the potential for interaction between atoms within a given volume of any given material, (σ_a), can be calculated as:

$$ACS = \sigma_a = \frac{N}{N_A}(\mu/\rho) \tag{7}$$

The electronic cross section (ECS), representing the probability of interaction between photons and electrons, is given by:

$$ECS = \sigma_e = \frac{\sigma_a}{Z_{eff}} \tag{8}$$

In the analysis of compounds composed of multiple elements, the atomic number of the resulting compound is designated as Z_{eff}. Z_{eff} is found with the help of Eqs. (7) and (8) as:

$$Z_{eff} = \frac{\sigma_a}{\sigma_e} \tag{9}$$

The EBF and EABF can be calculated using the formulas provided in Refs. [25, 26]. The geometric progression (G-P) fitting parameters can be obtained from Ref. [27] and used in Eq. (11). EBF and EABF can be obtained using Eq. (12) or (13) by determining K(E,x) from Eq. (14), where a, b, c, d, and X_k are the exposure G-P fitting parameters, and x is thickness in mean free path (mfp). The ratio (R) of the Compton partial mass attenuation coefficient (MAC) to the total MAC can be determined for the material at a given photon energy. R_1 and R_2 denote the $(\mu m)_{\text{Compton}}/(\mu m)_{\text{Total}}$ ratios of these two adjacent elements with atomic numbers Z_1 and Z_2. F_1 and F_2 are the corresponding G-P fitting parameters for these elements at a specific energy. X and E indicate the depth of penetration and the initial energy of the photon, respectively. The combination of K (E, X) and X represents the photon multiplication dose and defines the spectral shape [22].

$$Z_{eq} = \frac{Z_1(logR_2 - logR) + Z_2(logR - logR_1)}{logR_2 - logR_1} \tag{10}$$

$$F = \frac{F_1(logZ_2 - logZ_{eq}) + F_2(logZ_{eq} - logZ_1)}{logZ_2 - logZ_1} \tag{11}$$

$$B(E,x) = 1 + \frac{(b-1)(K^x - 1)}{(K-1)} \text{ for } K \neq 1 \tag{12}$$

$$B(E,x) = 1 + (b-1)x \text{ for K} = 1 \tag{13}$$

$$K(E,x) = cx^a + d\,\frac{\tanh\left(\frac{x}{X_k} - 2\right) - \tanh(-2)}{1 - \tanh(-2)}$$

$$\text{for } x \leq 40 \text{ mfp} \tag{14}$$

The FNRCS ($\sum R$) values of the compounds are defined by the following equation [22]:

$$\sum R = \sum_i \rho_i \left(\sum R/\rho\right)_i \tag{15}$$

where ρ_i and $(\sum R/\rho)_i$ are the mass RCS and partial density of the compound of the i$^{\text{th}}$ constituent element, respectively.

The crystallite size is calculated by the diffraction pattern depending on the full width half height (FWHM) and the Debye-Scherrer equation [28]. Here, β is the FWHM in radians, K is the Scherrer's constant (≅ 0.9), d is the average size of the crystalline, λ is the X-ray wavelength, and θ is the Bragg angle in degrees [16]:

$$d = \frac{K\lambda}{\beta cos\theta} \qquad (16)$$

3. Results and Discussion

3.1. EDS and SEM Analysis

The SEM images of the samples are given in Fig. 2. If the micrographs obtained from the surfaces of the samples are studied, smooth surfaces with some microcrystallites are seen. From the micrographs of the samples with Ta and W additions, the structures represent α-Ta, β-Ta, and α-W structures. It is obvious that Ta and W, due to their high melting points and densities, gather in some locations and thus affect the homogeneous structure of the samples.

The EDS spectra are given in Figs. 3-6, and the weight % ratios of the elements obtained from these spectra are given in Table 2. It is understood from both the mapping images and the EDS analyses that the most homogeneous structure is in the A and X samples. EDS analysis results were found to be consistent except for the B3 and X3 samples for the W amount. As a result of selecting a certain area for measurement during EDS mapping analysis, the area in question is not completely homogeneous, and W shows the feature of clumping during the melting process of the material. Since Ta and W possess considerably higher melting points than the other constituent elements, their incomplete dissolution during the casting process can lead to compositional inhomogeneities. Consequently, the EDS results for Ta and W show acceptable but slightly different values from the nominal casting ratios, likely due to limited solubility and uneven element distribution.

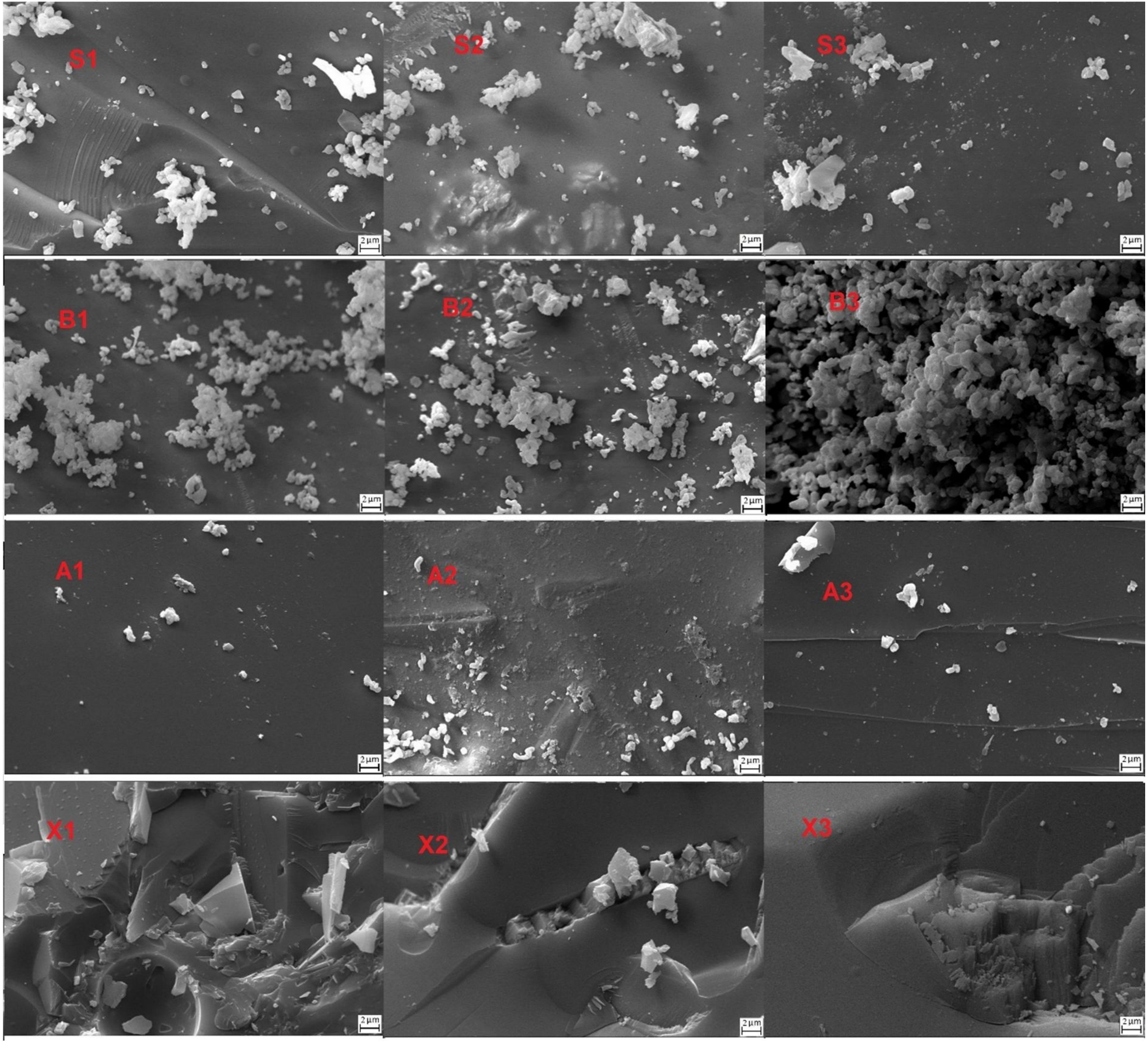

FIG. 2. SEM images of the samples.

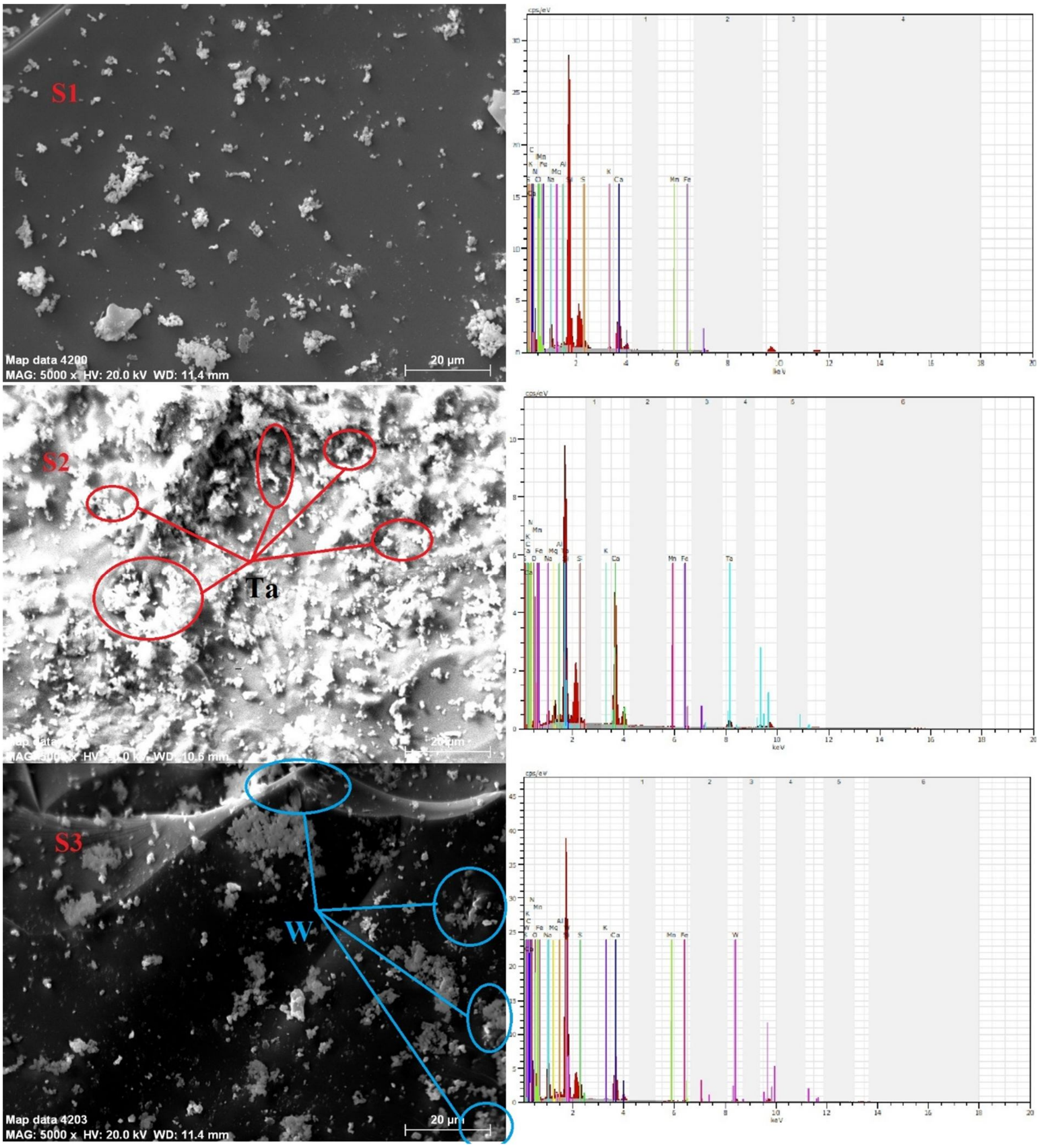

FIG. 3. The results of EDS for the S group samples.

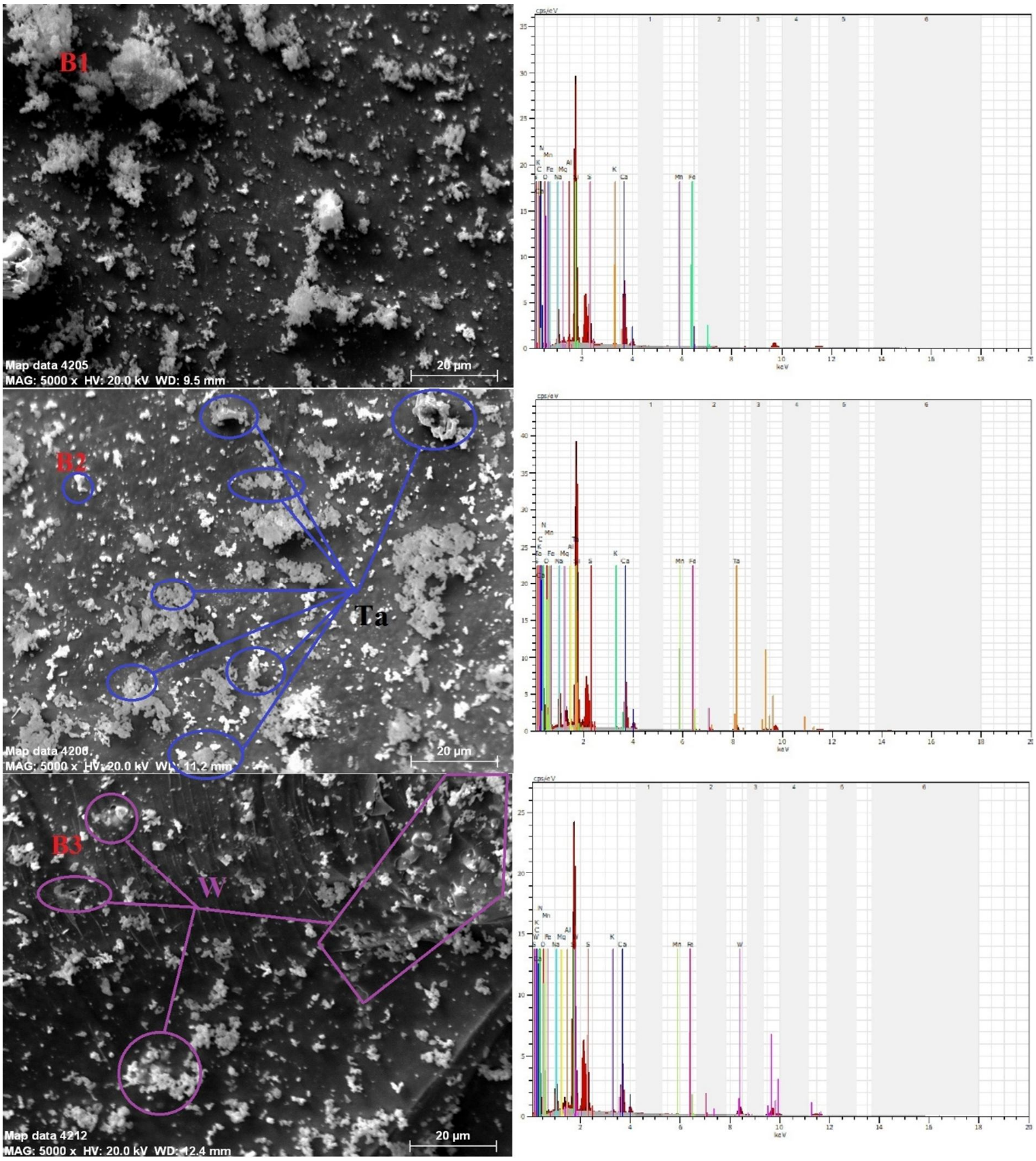

FIG. 4. The results of EDS for the B group samples.

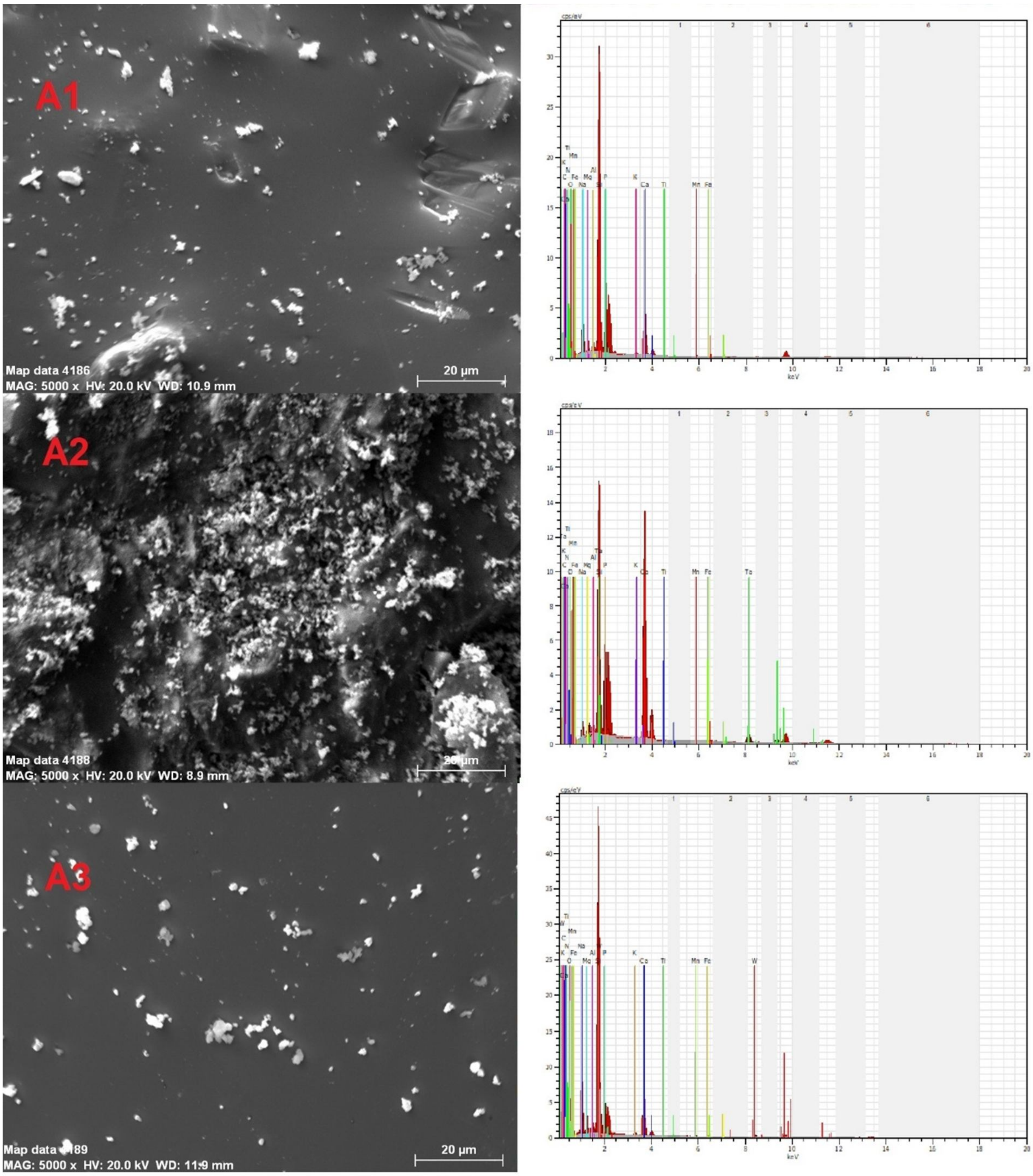

FIG. 5. The results of EDS for the A group samples.

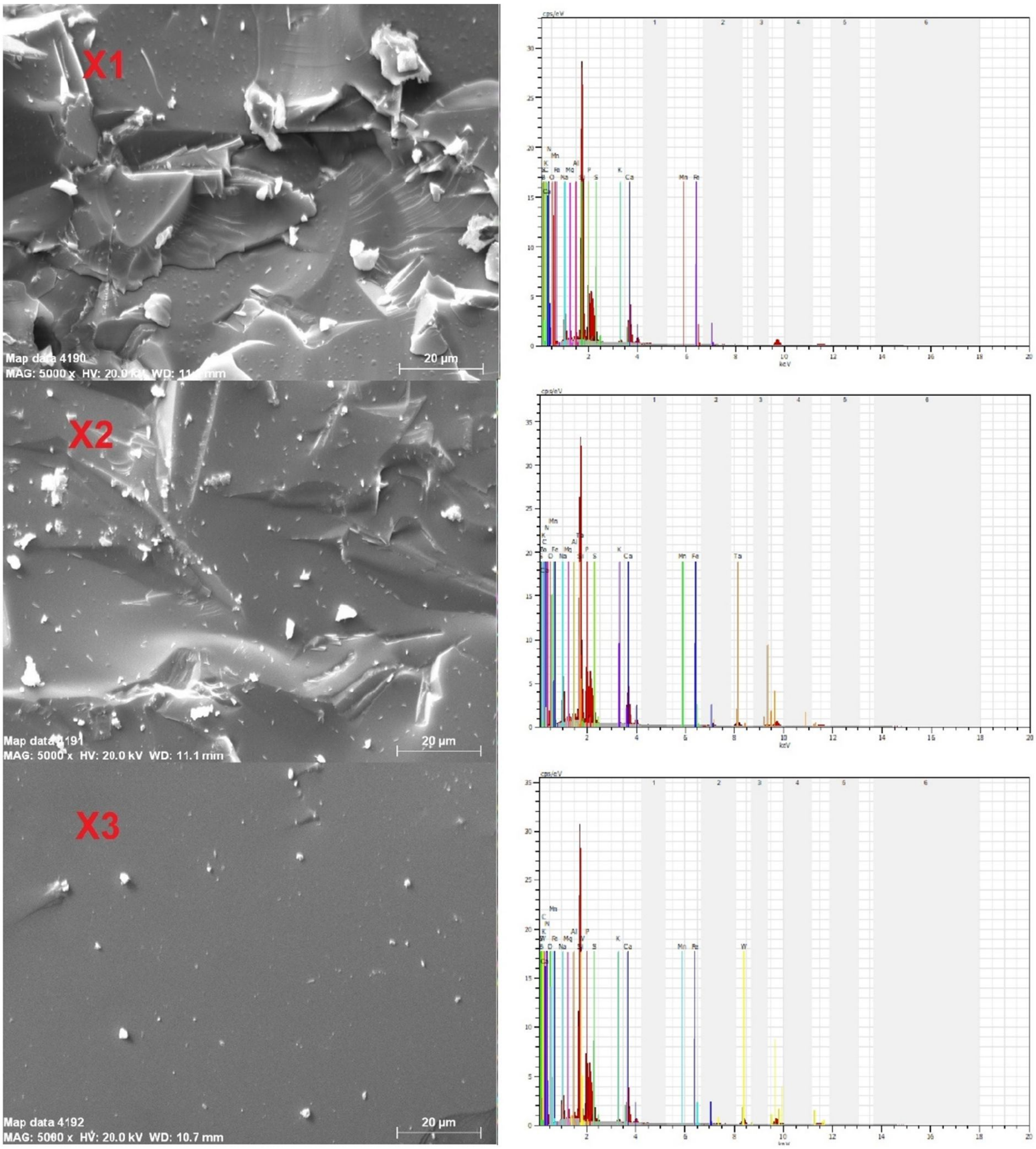

FIG. 6. The results of EDS for the X group samples.

TABLE 2. EDS results of the samples determined in the SEM images.

Samples	O	C	Ca	K	Si	Na	Fe	Ti	Mg	S	P	Al	B	N	Mn	Ta	W	Density
S1	45.10	1.21	10.86	0.33	24.37	5.53	0.37	-	0.56	5.06	-	0.71	-	5.77	0.14	-	-	1.645
S2	48.60	2.05	22.82	0.14	1.03	3.52	0.23	-	0.90	0.85	-	1.20	-	6.49	0.22	11.94	-	2.567
S3	39.27	1.12	11.02	0.39	19.26	9.78	0.29	-	1.38	2.83	-	1.23	-	3.12	0.16	-	10.14	2.566
B1	42.59	1.11	14.38	0.24	23.68	6.06	0.35	-	0.68	5.72	-	0.84	-	4.18	0.17	-	-	1.647
B2	51.68	1.84	10.45	0.28	5.00	9.55	0.21	-	1.20	0.95	-	1.36	-	4.60	0.12	12.76	-	2.695
B3	34.55	2.01	9.91	0.35	13.61	5.81	0.25	-	0.78	6.18	-	0.93	-	5.16	0.13	-	20.33	3.722
A1	44.30	1.62	8.45	0.24	23.83	6.27	0.42	0.13	1.26	-	11.6	1.32	-	0.25	0.30	-	-	1.678
A2	35.31	4.98	29.22	0.1	7.54	0.47	0.38	0.08	0.54	-	7.91	0.58	-	-	0.12	11.87	-	2.611
A3	36.86	1.01	8.02	0.43	24.54	11.63	0.25	0.06	2.27	-	5.78	1.68	-	0.01	0.10	-	7.36	2.321
X1	38.99	1.24	8.47	0.34	22.36	6.28	0.35	-	1.09	1.74	8.01	1.07	6.06	3.89	0.14	-	-	1.664
X2	27.04	0.93	9.35	0.39	21.37	6.94	0.28	-	1.21	2.05	9.98	1.18	1.59	4.12	0.14	13.42	-	2.939
X3	20.80	1.10	8.29	0.57	23.16	5.27	0.40	-	0.96	2.87	11.81	0.90	3.15	4.15	0.18	-	16.39	3.384

3.2. XRD Analysis

The room-temperature XRD patterns are displayed in Fig. 7. The observed diffraction peaks were evaluated by the literature [16, 29-34]. The X-ray analyses of the S and B groups reveal similar properties and the presence of α-Ta, β-Ta, α-W, calcite, and ferrite main phase peaks. The **S2** and **B2** samples, which were produced with Ta addition, exhibit dominant α-Ta and β-Ta. The S3 and B3 samples produced by W addition give the α-W main phase. It is observed that the A and X groups show more amorphous structure in XRD patterns. In the S and B group samples, both amorphous and crystalline features are determined.

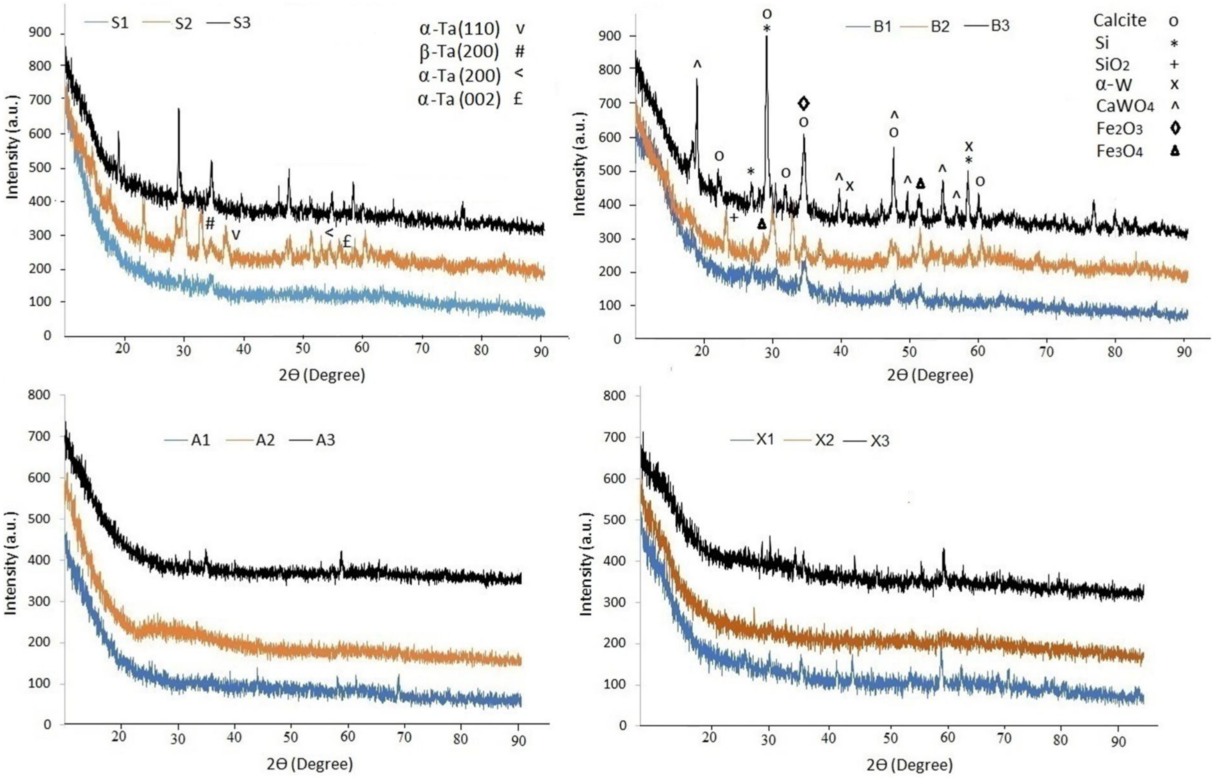

FIG. 7. XRD patterns of the samples.

The presence of the α-Ta main phase at ≈ 36°, seen in the X-ray spectra of the S2 and B2, corresponds to a crystallite size of 20.42 nm for $\beta = 0.428$. In the S3 and B3 samples, the α-W main phase at ≈ 40° has a crystallite size of 41.51 nm for $\beta = 0.213$. The crystallite size of the other main phase at ≈ 29° assigned to calcite is 27.46 nm for $\beta = 0.318$.

The relationship between crystallite size and grain size suggests that variations in crystallite size directly influence grain size. Consistently, the B3, which exhibits the largest crystal size among the samples, as determined by SEM images, also shows the largest grain size in SEM images. This correlation confirms that the calculated crystallite sizes align well with the grain size observations from SEM analysis.

3.3. EPR Study

EPR is a method used to detect paramagnetic centers in materials under the influence of an external magnetic field. The EPR resonance condition is expressed by the equation hυ = gβH, with g-value, where β is the Bohr magneton, H is the magnetic field, h is Planck's constant, and υ is the microwave frequency. This equation is used for the determination of the values. In EPR spectra, centers can originate from both crystalline and glassy regions of the material. The g-factor characterizes the paramagnetic center by indicating the effect of the local magnetic field on unpaired electrons; hence, it provides information about the orbital nature of these electrons and the type of paramagnetic center present [35]. The room-temperature EPR spectrum common to all samples is shown in Fig. 8. Fe^{+3} ions or high-spin isolated Fe^{+3} in the structure are determined with a g value of ≈ 4.21

for the samples [36]. The line was observed to be similar for all the studied samples; therefore, the spectrum of S3 is shown in Fig. 8. In general, it is expected to observe six hyperfine lines of Mn^{+2} in the EPR spectrum, but in this study, a broad EPR signal with a g-value of ≈ 1.996, which can be assigned to Mn+2 (I = 5/2) was observed. This broad signal can be the result of the random and close localization of Mn ions and their dipole-dipole or exchange interactions [37].

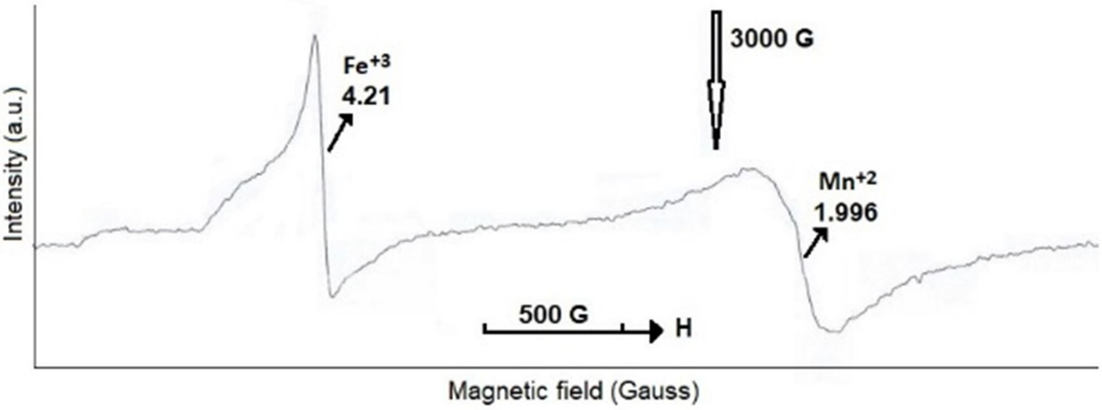

FIG. 8. EPR spectrum of the sample S3.

3.4. Radiation Protection Analysis

The Phy-X/PSD code was used to calculate radiation attenuation parameters based on the chemical compositions (w%) of the samples determined by EDS (Table 2). The variation of MAC with photon energy (1 keV–100 GeV) is shown in Fig. 9(a). The behavior in low, medium, and high energy regions corresponds to the photoelectric effect (PE), Compton scattering (CS), and pair production (PP), respectively, which influence the observed changes in MAC. To validate the results, XCom [38] calculations were also performed, showing good agreement with the Phy-X/PSD values. The MAC values at representative low, medium, and high energies calculated by both methods are listed in Table 3. The LAC values changed with photon energies (1keV-100GeV), as demonstrated in Fig. 9(b). Since LAC depends on the material density and MAC, the LAC values of all samples are observed to be similar across the energy range. Additionally, the samples' MAC results were compared with previously reported values for ordinary concrete (OC) [39] and cement [40], as shown in Fig. 9(c). At low photon energies, the MAC values (and consequently the shielding efficiencies) of the samples can be ordered as follows: B3 > X3 > A2 > X2 > S2 > B2 > S3 > A3 > Cement > B1 > A1 > S1 > X1 > OC. At high photon energies, the shielding efficiency ranking of the samples is as follows: B3 > X3 > A2 > X2 > S2 > B2 > Cement > A3 > S3 > B1 > A1 > S1 > X1 > OC. Among the samples with W addition, the B and X groups exhibit higher shielding performance, while among the samples with Ta addition, the A and X groups show better protection. Interestingly, the B and A samples without Ta or W also demonstrate higher shielding efficiency than the remaining samples. Across all energy ranges, a common observation is that all prepared samples outperform OC in radiation protection.

The variations of mean free path (MFP) and half-value layer (HVL) with photon energy are shown in Fig. 10(a)-10(b). Materials with lower HVL and MFP values are considered better shields. The B3 sample exhibits the lowest MFP and HVL values, indicating the highest shielding potential, while the X1 sample shows the highest MFP and HVL values. Based on HVL values, the order of shielding efficiency for all samples is: B3 > X3 > X2 > A2 > S2 > B2 > S3 > A3 > A1 > B1 > S1 > X1. The radiation shielding capabilities of the samples were also compared with OC and cement (Fig. 10c). It is evident that samples numbered two and three consistently have lower HVL values than OC and cement, whereas the first-numbered samples exhibit lower shielding efficiency than these conventional materials.

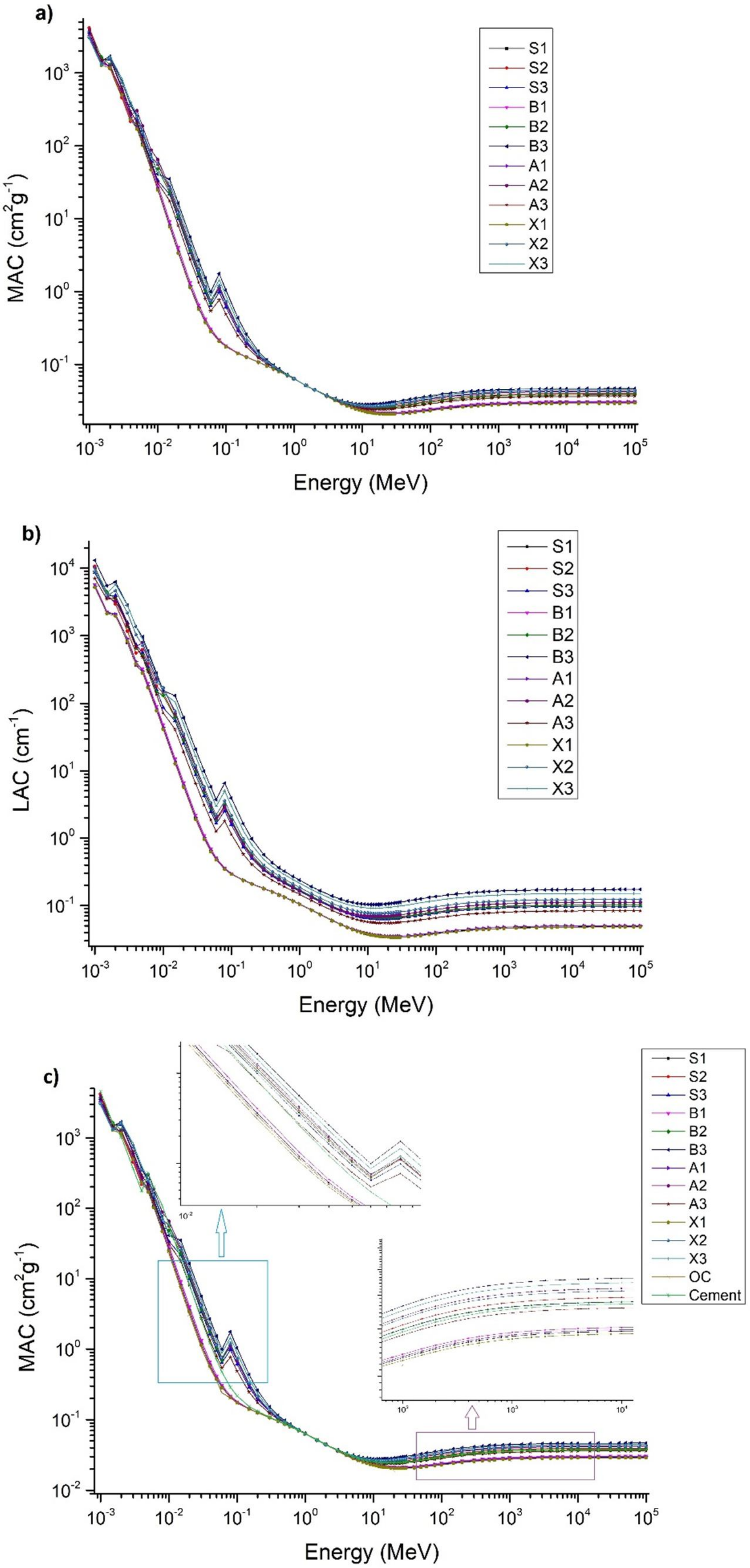

FIG. 9. The dependence of (a) MAC, (b) LAC, and (c) comparison of MAC values with OC and cement on photon energies.

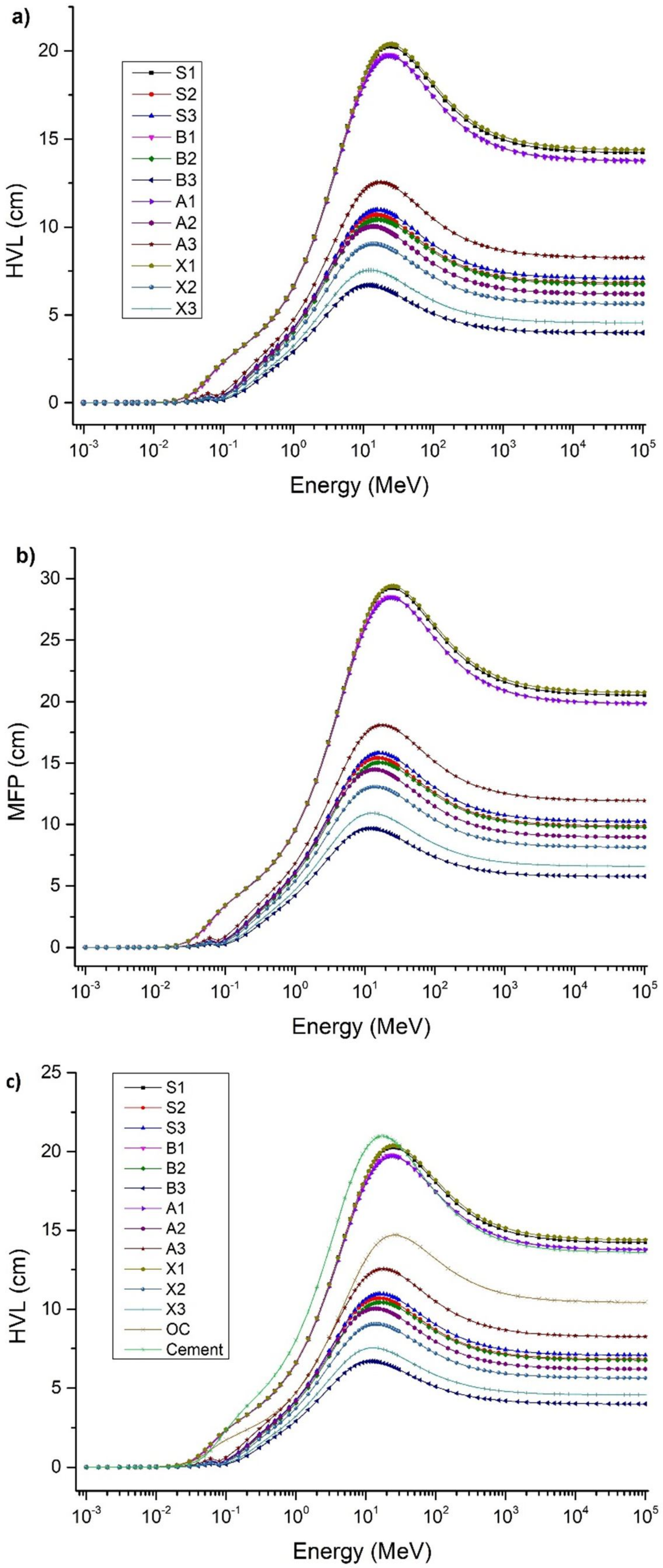

FIG. 10. The dependence of (a) HVL, (b) MFP, and (c) the comparison of HVL values with OC and cement on photon energies.

TABLE 3. MAC values of the samples obtained by Phy-X/PSD and XCom for some energies.

	1.5 x10^{-3} (MeV)	1.5 x10^{-2} (MeV)	1.5 x10^{-1} (MeV)	1.5 x10^{0} (MeV)	1.5 x10^{1} (MeV)	1.5 x10^{2} (MeV)	1.5 x10^{3} (MeV)
S1 Phy-x/PSD	1351.6	8.164	0.143	0.052	0.021	0.025	0.029
S1 Xcom	1351.0	8.163	0.143	0.052	0.021	0.025	0.029
S2 Phy-x/PSD	1597.6	24.62	0.310	0.052	0.025	0.033	0.038
S2 Xcom	1508.0	23.41	0.300	0.052	0.025	0.032	0.038
S3 Phy-x/PSD	1523.1	21.52	0.288	0.051	0.025	0.032	0.037
S3 Xcom	1526.0	21.57	0.288	0.051	0.025	0.032	0.037
B1 Phy-x/PSD	1378.1	9.201	0.144	0.052	0.022	0.025	0.029
B1 Xcom	1378.0	9.201	0.144	0.052	0.022	0.025	0.029
B2 Phy-x/PSD	1650.0	22.78	0.318	0.051	0.025	0.032	0.037
B2 Xcom	1650.0	22.78	0.320	0.051	0.025	0.032	0.037
B3 Phy-x/PSD	1471.3	34.96	0.435	0.051	0.028	0.039	0.045
B3 Xcom	1471.0	34.96	0.435	0.051	0.028	0.039	0.045
A1 Phy-x/PSD	1333.9	8.224	0.142	0.051	0.021	0.025	0.029
A1 Xcom	1334.0	8.225	0.142	0.051	0.021	0.025	0.029
A2 Phy-x/PSD	1447.8	27.54	0.312	0.051	0.026	0.035	0.041
A2 Xcom	1448.0	27.54	0.312	0.051	0.026	0.035	0.041
A3 Phy-x/PSD	1493.7	17.69	0.248	0.051	0.024	0.030	0.035
A3 Xcom	1494.0	17.69	0.025	0.051	0.024	0.030	0.035
X1 Phy-x/PSD	1278.8	7.704	0.141	0.051	0.021	0.024	0.028
X1 Xcom	1278.0	7.702	0.141	0.051	0.021	0.024	0.028
X2 Phy-x/PSD	1335.6	25.89	0.329	0.051	0.026	0.035	0.040
X2 Xcom	1336.0	25.91	0.329	0.051	0.026	0.035	0.040
X3 Phy-x/PSD	1260.8	30.83	0.379	0.051	0.027	0.037	0.043
X3 Xcom	1261.0	30.83	0.379	0.051	0.027	0.037	0.043

The variation of Z_{eff} values versus photon energy is shown in Fig. 11. In the low-energy region, due to the PE cross-section (Z^{4-5}), the Z_{eff} values are the highest. In the mid-energy region, based on the change of CS cross-section ($E^{-3.5}$), a rapid decrease is determined. In the high-energy region, because of the variation of the PP cross-section (Z^2), the values increase slightly and then remain constant [41]. The Z_{eff} values are affected by the presence of elements with different atomic numbers within the material. Since Z_{eff} is the atomic number of the material, including more than one element, structures with large atomic number differences cause fluctuations. Samples numbered two and three, which contain Ta and W, show the highest Z_{eff} values and the most pronounced fluctuations. Consequently, B3 and X3 exhibit the highest shielding performance, while S1 and X1 show the lowest, based on Z_{eff} values.

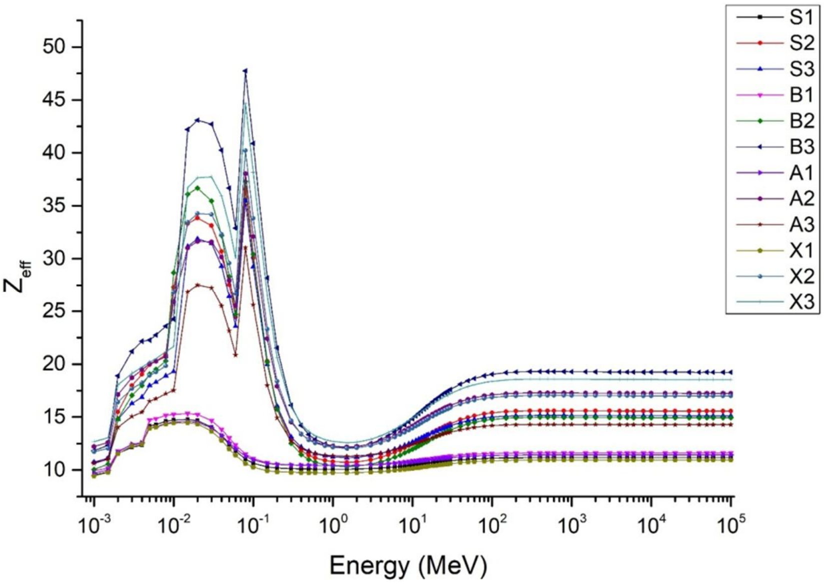

FIG. 11. The dependence of Z_{eff} on photon energies.

The EABF is the buildup factor related to the energy absorbed or deposited in the interacting material. On the other hand, EBF is another type of buildup factor in which there is an exposure to interacting material. The dependence of EBF and EABF on photon energies is illustrated in Figs. 12-13. In the low-energy region, EBF and EABF have lower values based on the PE, whereas in the mid-energy region, they have their highest values based on CS due to the scattered large number of photons. In the high-energy region, the PP effect causes strong photon absorption, and EBF and EABF decrease [41]. According to the obtained EBF and EABF values, the photons cluster relatively higher in X1 and A1 samples and lower in B3 and X3. Therefore, it is noted that the CS process is dominantly seen for X1 and A1 samples.

The samples' fast neutron shielding capabilities were also established by Phy-X/PSD, and the cross-sections are given in Fig. 14. As seen in the figure, the highest neutron attenuation is achieved for B3 and X3, the lowest attenuation is for B1, S1, and A1. It can also be concluded that FNRCS values of B3 and X3 are better than that those of the previously reported OC.

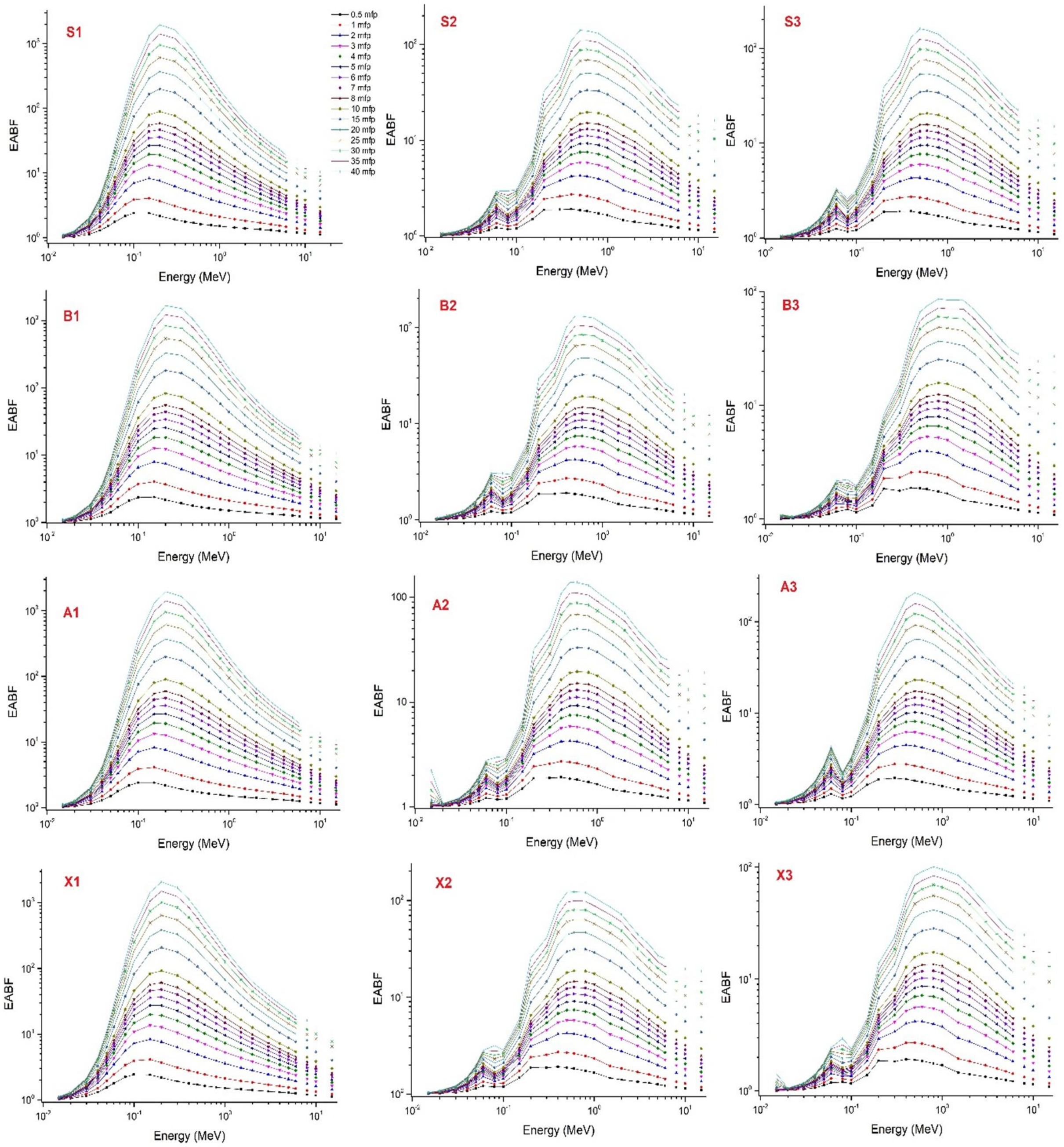

FIG. 12. The dependence of EABF values on photon energies.

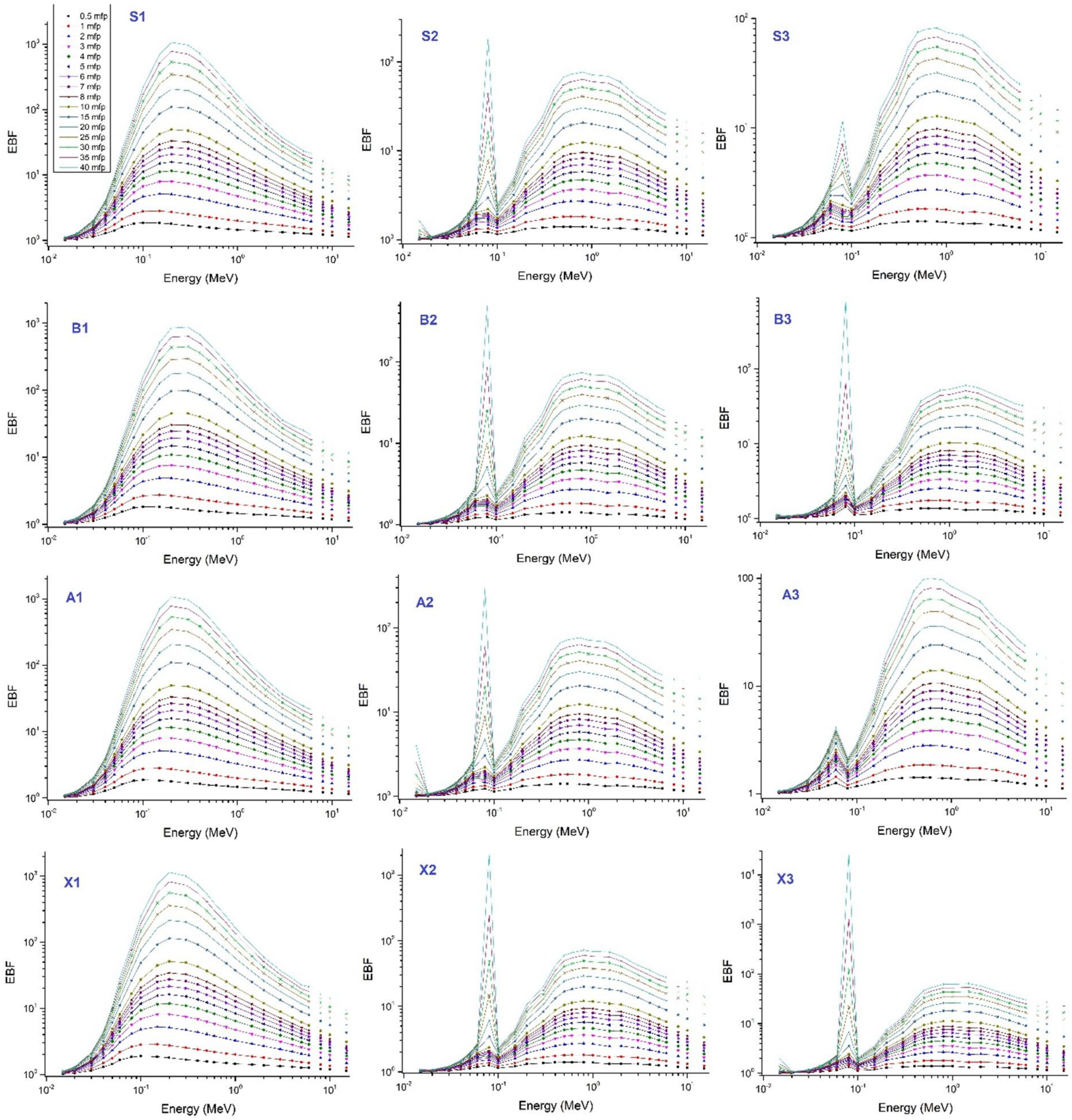

FIG. 13. The dependence of EBF values on photon energies.

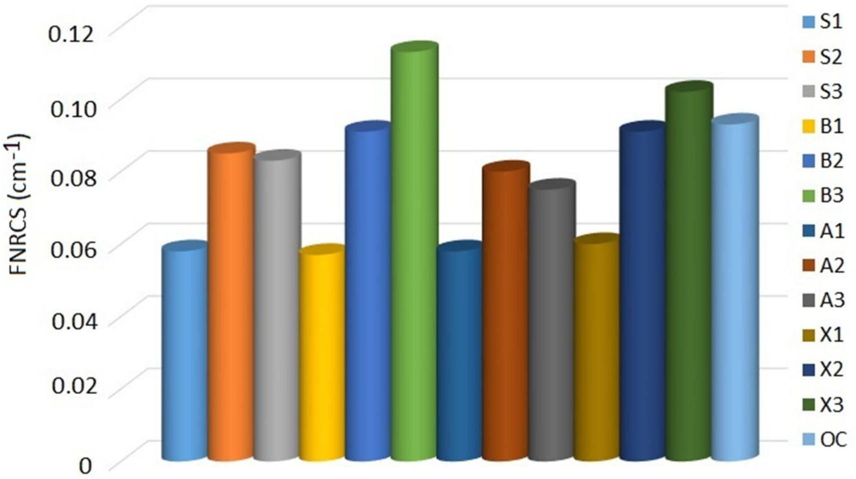

FIG. 14. The FNRCS values of the samples.

4. Conclusion

The motivation of this study was to produce alternative materials by reusing waste, aiming to achieve higher RSC. In accordance with this purpose, RSC and structural features of the waste samples were determined by Phy-X/PSD code and spectroscopic techniques. The EPR spectra revealed a signal with a g-value of 4.21, which is assigned to the ferric center. Using the Debye-Scherrer equation, crystallite sizes of the main phases were calculated based on the XRD spectra. Both EDS analysis and elemental mapping indicate that the A and X groups exhibit the most homogeneous structures. Based on the computational results of radiation shielding parameters, it is noteworthy to emphasize that the existence of heavy metal Ta and W contents with higher atomic number in the sample advances the RSCs of the material. The addition of Ta and W to the samples can also improve the mechanical features, such as tensile strength and durability of the materials. In addition, it can be said that the neutron attenuation capacity of B3 and X3 is the highest, similar to their photon attenuation capacity. Among the samples numbered one, B1 has the highest RSC, and X1 has the lowest. X2 is the most effective shield, and B2 the least among the samples numbered two. RSC of B3 is the highest, while that of A3 is the lowest within the samples numbered three. Overall, all designed waste-based samples show promise as novel radiation shielding materials. Future studies focusing on mechanical properties, such as elasticity and tensile strength through measurements of Young’s modulus or Poisson’s ratio, would provide additional valuable insights into the applicability of these materials.

Acknowledgement

Experimental results were obtained from the Advanced Technology Research & Application Center (ILTEK) of Selcuk University.

Competing Interests

The authors declare that they have no known competing financial interests or personal relationships that could have appeared to influence the work reported in this paper.

Ethics Approval

Not applicable

Consent to Participate

Not applicable

Consent for Publication

Not applicable

Author Contributions

All authors contributed to the study conception and design. Material preparation, data collection, and analysis were performed by Murat AYGUN and Zeynep AYGUN. The first draft of the manuscript was written by Zeynep AYGUN, and all authors commented on previous versions of the manuscript. All authors read and approved the final manuscript.

Availability of Data and Materials

Data from this study are available from the corresponding author on responsible request.

Funding

This work was supported by Bitlis Eren University Scientific Research Projects Coordination Unit (BEBAP) with a project grant number 2023.14.

References

[1] Islam, G.M.S., Rahman, M.H., and Kazi, N., Int. J. Sustain. Built. Environ., 6 (1) (2017) 37.

[2] Imbabi, M.S., Carrigan, C., and McKenna, S., Int. J. Sustain. Built. Environ., 1 (2) (2012) 194.

[3] Detwiler, R., Bhatty, J.I., and Bhattacharja, S., "Supplementary Cementing Materials for Use in Blended Cements", (Research and Development Bulletin Rd112t, Portland Cement Association, Skokie, Illinois, USA, 1996).

[4] Eid, M.S., Bondouk, I.I., Saleh, H.M., Omar, K.M., Sayyed, M.I., El-Khatib, A.M., and Elsafi, M., Nucl. Eng. Technol., 54 (4) (2022) 1456.

[5] Kim, I.S., Choi, Y.S., Choi, S.Y., and Yang, E.I., Ann. Nucl. Energy, 133 (2019) 750.

[6] Binici, H., Aksogan, O., Sevinc, A.H., and Cinpolat, E., Constr. Build. Mater., 93 (2015) 1145.

[7] Nassar, R.U.D. and Soroushian, P., Constr. Build. Mater., 29 (2012) 368.

[8] Ryou, J., Shah, S.P., and Konsta-Gdoutos, M.S., Adv. Appl. Ceram. Struct. Funct. Bioceram., 105 (6) (2006) 274.

[9] Rashad, A.M., Constr. Build. Mater., 72 (2014) 340.

[10] Taha, B. and Nounu, G., J. Mater. Civ. Eng., 21 (12) (2009) 709.

[11] Khazaalah, T.H. et al., J. Mater. Res. Technol., 19 (2022) 3355.

[12] Jasmine, J.N.Z., Ramzun, M.R., Zahirah, N.A.N., Azhar, A.R., Hana, M.A.M., Zakiah, Y.N., and Yasmin, M.R., J. Phys. Conf. Ser., 1497 (1) (2020) 012010.

[13] Mancı, A. and Sarıışık, A., Civiltech., 2019 (2019) 124.

[14] Ince, C. and Derogar, S., Emerg. Mater. Res., 7 (2) (2018) 118.

[15] Khazaalah, T.H., Mustafa, I.S., and Sayyed, M.I., Nucl. Eng. Technol., 54 (12) (2022) 4708.

[16] Aygun, M., Aygun, Z., and Ercan, E., Radiat. Phys. Chem., 212 (2023) 111147.

[17] Sayyed, M.I., Almurayshid, M., Almasoud, F.I., Alyahyawi, A.R., Yasmin, S., and Elsafi, M., Mater. (Basel), 15 (23) (2022) 8371.

[18] Aygun, Z., Aygun, M., and Yarbasi, N., J. New Results Sci., 10 (2021) 46.

[19] Elsafi, M., Almousa, N., Al-Harbi, N., Almutiri, M.N., Yasmin, S., and Sayyed, M.I., J. Mater. Res. Technol., 22 (2023) 269.

[20] Aygun, Z. and Aygun, M., Int. J. Environ. Sci. Technol., 19 (2022) 5675.

[21] Karpuz, N., J. Radiat. Res Appl. Sci., 16 (4) (2023) 100689.

[22] Sakar, E., Ozpolat, O.F., Alım, B., Sayyed, M.I., and Kurudirek, M., Radiat. Phys. Chem., 166 (2020) 108496.

[23] Xiang, C. et al., Intermetal., 104 (2019) 143.

[24] Jackson, D.F. and Hawkes, D.J., Phys. Reports, 70 (1981) 169.

[25] Harima, Y., Sakamoto, Y., Tanaka, S., and Kawai, M., Nucl. Sci. Engineer., 94 (1986) 24.

[26] Harima, Y., Radiat. Phys. Chem., 41 (1993) 631.

[27] ANSI/ANS 643. "Gamma-ray Attenuation Coefficients and Buildup Factors for Engineering Materials", (American Nucl. Soc., La Grange Park, Illinois, 1991).

[28] Scherrer, P., Röntgenstrahlen Nachr Ges Wiss Göttingen, 26 (1918) 98.

[29] Noval, V.E. and Carriazo, J.G., Mater. Res., 22 (3) (2019) e20180660.

[30] Brar, L.K., Singla, G., Kaur, N., and Pandey, O.P., J. Therm. Anal. Calorim., 119 (2015) 175.

[31] Moharana, P.L., Anwar, S., Islam, A., and Anwar, S., Perspectives in Sci., 8 (2016) 636.

[32] El-Mahllawy, M.S., Kandeel, A.M., Abdel Latif, M.L., and El Naga, A.M., Recycling, 3 (2018) 39.

[33] Aygun, Z. and Yarbasi, N., Karaelmas Sci. Engineer. J., 9 (2) (2019) 215.

[34] Polini, R., Marcucci, A., D'Ottavi, C., Nunziante, P., De Filippis, P., and Marcheselli, G., ACS Sustain. Chem. Eng., 9 (25) (2021) 8458.

[35] Filek, M., Łabanowska, M., Kurdziel, M., and Sieprawska, A., Toxins (Basel), 9 (6) (2017) 178.

[36] Aygun, Z. and Aygun, M., Spectrochim. Acta A, 166 (2016) 73.

[37] Markevich, I., Korsunska, N., Stara, T., Vorona, I., Melnichuk, O., Venger, Y., and Khomenkova, L., J. Mater. Sci. Mater. Electron., 34 (2023) 646.

[38] Berger, M.J. and Hubbell, J.H., "XCOM: Photon Cross Sections Database", (Web Version 12 National Institute of Standards and Technology Gaithersburg, MD 20899 USA, 1987).

[39] Bashter, I.I., Ann. Nucl. Energy, 24 (17) (1997) 1389.

[40] Sathiparan, N. and De Zoysa, H.T.S.M., J. Build. Eng., 19 (2018) 216.

[41] Aygun, Z. and Aygun, M., Acta Phys. Polonica A, 5 (141) (2022) 507.